Check for updates

Overlayer deposition-induced control of oxide ion concentration in SrFe$_{0.5}$Co$_{0.5}$O$_{2.5}$ oxygen sponges†

Joonhyuk Lee, [ID][a] Younghak Kim, [ID][b] Jinhyung Cho,[c] Hiromichi Ohta [ID]*[d] and Hyoungjeen Jeen [ID]*[ae]

Controlling the oxide ion (O^{2-}) concentration in oxides is essential to develop advanced ionic devices, *i.e.* solid oxide fuel cells, smart windows, memory devices, energy storage devices, and so on. Among many oxides several transition metal (TM)-based perovskite oxides show high oxide ion conductivity, and their physical properties show high sensitivity to the change of the oxide ion concentration. Here, the change in the oxide ion concentration is shown through the overlayer deposition on the SrFe$_{0.5}$Co$_{0.5}$O$_{2.5}$ (SFCO) oxygen sponge film. We grew SFCO films followed by the deposition of two kinds of complex oxide films under exactly the same growth conditions, and observed the changes in the crystal structure, valence states, and magnetic ground states. As the NSMO overlayer grows, strong evidence of oxidation at the O K edge is shown. In addition, the Fe^{4+} feature is revealed, and the electron valence state of Co increased from 3 to 3.25. The oxide ion concentration of SFCO changes during layer growth due to oxidation or reduction due to differences in chemical potential. The present results might be useful to develop advanced ionic devices using TM-based perovskite oxides.
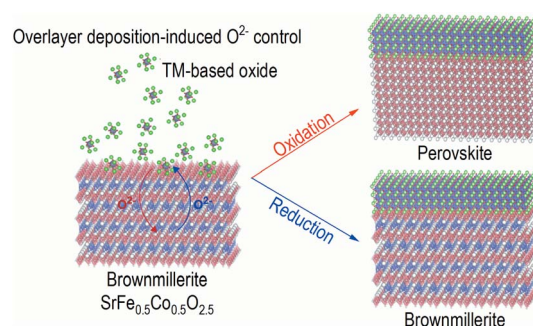
1. Introduction

The functional properties of complex metal oxides are influenced by lattice, spin, orbital, charge degrees of freedom, and their interplay.[1–7] The functionality is often realized by substrate induced strain, cation doping, and charge doping through interfacial engineering. Another promising method for controlling such functionality in complex metal oxides is to manipulate oxide ion concentration in the oxides.[8–13] Due to the known high oxide ion conductivity and excellent catalytic activity without triple phase boundaries, perovskite and perovskite-like structures are suitable choices for ion-driven technology.[13,14] The oxide ion-driven technology is important for ion conduction, the center of many energy storages such as magnetic memory devices,[15,16] fuel cells,[13,17] smart windows,[18] and sensor technology.[19]

Typically, functional devices, *i.e.* neuromorphic devices, solid oxide fuel cells, and *etc.*, are designed as a stack of several layers. It is often found that functional properties of each layer in the stack

are deviated from those of its bulk-form.[20,21] For example, due to modulation of interfacial chemistry, when certain oxides form heterostructures, reduced spin transport in La$_{1-x}$Sr$_x$MnO$_3$-based tunneling devices and unconventional transport behavior in LaNiO$_3$ due to unidirectional oxygen diode effect are observed.[22,23] In addition, heterointerface design is crucial for performance and longevity of electrochemical devices from the example of an oxide getter for detoxicating contaminated air and enhanced oxygen surface exchange kinetics in fuel cell applications.[24,25] Therefore, it is indispensible to understand chemistry at the interface between the two oxides and track the changes in oxide ion concentration along depth direction.

Fig. 1 Schematic illustration of overlayer deposition-induced oxide ion concentration control in SFCO film. When STO is deposited on BM-SFCO film, reduction occurs. On the other hand, when NSMO is deposited on BM-SFCO, oxidation occurs and the crystal structure changes to perovskite.

[a]Department of Physics, Pusan National University, Busan 46241, Korea. E-mail: hjeen@pusan.ac.kr

[b]Pohang Accelerator Laboratory, Pohang University of Science and Technology, Pohang 37673, Korea

[c]Department of Physics Education, Pusan National University, Busan 46241, Korea

[d]Research Institute for Electronic Science, Hokkaido University, Sapporo 001-0020, Japan. E-mail: hiromichi.ohta@es.hokudai.ac.jp

[e]Research Center for Dielectric and Advanced Matter Physics, Pusan National University, Busan 46241, Korea

† Electronic supplementary information (ESI) available. See DOI: 10.1039/d1ra06378b

In this report, we studied modulation of interfacial chemistry of oxygen sponge SrFe$_{0.5}$Co$_{0.5}$O$_{2.5}$ (SFCO), which is a solid solution of SrFeO$_{2.5\pm\delta}$ and SrCoO$_{2.5+\delta}$. The crystal structure of the oxygen sponges can be reversibly converted between brownmillerite/perovskite upon redox reactions with various ways.[26–30] Brownmillerite structure is ABO$_{2.5}$, where A and B are cations and O is oxygen in chemical formula. It consists of alternate stacks of an octahedral layer and an oxygen deficient tetrahedral layer. A simple deposition of an overlayer on an SFCO oxygen sponge film changes the oxide ion concentration (Fig. 1). We fabricated SFCO films followed by the deposition of two different complex oxides, *i.e.* SrTiO$_3$ and Nd$_{0.5}$Sr$_{0.5}$MnO$_3$ films under exactly the same growth condition. We tracked the changes in the crystal structure, valence state, and magnetic ground state. As a result of these observations, the oxide ion concentration of SFCO readily changed during layer growth due to oxidation or reduction due to differences in chemical potentials. The results of this study on the interface of complex oxides can provide opportunities to improve the design and performance of new devices.

2. Experimental

2.1 Sample preparation

Brownmillerite SFCO (space group *icmm*, $a = 5.6243$ Å, $b = 15.6515$ Å, $c = 5.5017$ Å (ref. 31)) thin films (three samples) were grown on (001) (LaAlO$_3$)$_{0.3}$-(SrAl$_{0.5}$Ta$_{0.5}$O$_3$)$_{0.7}$ (LSAT) substrates by pulsed laser deposition (PLD). A Q-switched 3ω-Nd:YAG ($\lambda = 355$ nm) laser was used to ablate the ceramic targets. The laser fluence and repetition rate were kept as 0.75 J cm^{-2} and 4 Hz, respectively. Optimal growth conditions were selected by controlling the substrate temperature and oxygen partial pressure (P_{O_2}), and as-grown SFCO (SFCO) shows the best crystallinity at $T = 600$ °C and $P_{O_2} = 100$ mTorr with brownmillerite structure. One sample was cooled below 50 °C under the same P_{O_2} after the film growth. An overlayer of either SrTiO$_3$ (STO) or Nd$_{0.5}$Sr$_{0.5}$MnO$_3$ (NSMO) was deposited on each SFCO sample under the same PLD condition without breaking vacuum. Then, these two samples, *i.e.* NSMO/SFCO and STO/SFCO, were cooled below 50 °C under the same P_{O_2} after the film growth.

In order to exclude other influences during the deposition of the overlayer, the target was rotated and replaced while maintaining the same deposition state after the growth of the SFCO. Only the overlayer deposition induced a phase transition from brownmillerite to perovskite structure. A detailed discussion of phase transitions will be provided later. The deposition time was adjusted to control the thickness of each layer. After depositing individual SFCO, STO, and NSMO thin films, the thickness and deposition rate were determined by the X-ray reflectivity followed by the simulation/fitting analysis. Through the deposition rate obtained through analysis, SFCO was controlled to be eight unit cells in brownmillerite notation, while STO and NSMO were controlled to be four unit cells.

2.2 Characterization

2.2.1 X-ray diffraction. Before studying the interface between the two layers, non contact atomic force microscopy observation (AFM, SPA 400, Seiko) was performed to ensure that each layer was deposited flat. The root mean square roughness of the as-grown SFCO is 0.4 nm, and the roughness values of the overlayered SFCOs were 0.7 nm or less as shown in Fig. S1.† We conducted X-ray diffraction (XRD, D8 discover, Bruker, Cu Kα_1, $\lambda = 1.5406$ Å) to analyze the crystal structure of each sample. We could calculate the changes in the lattice constant through the 2θ–ω scan and reciprocal space mapping (RSM) around (103) Bragg reflection of LSAT substrates depending on the overlayers.

2.2.2 X-ray absorption. X-ray absorption spectroscopy (XAS) with total electron yield (TEY) mode was performed to determine the valence states of SFCO thin films at 300 K and under 10^{-9} torr at the 2A beamline of the Pohang Accelerator Laboratory. The probing depth of TEY mode is about 5 to 10 nm, so the spectrum comes out completely from the top of the film. Surface-sensitive XAS mode was chosen, since the overlayer thickness is four unit cells. In addition, the beam incidence angle was set to 45° to observe the valence state changes in the buried oxygen sponge SFCO.

2.2.3 Magnetization. Magnetization *versus* temperature (M–T) curves were measured to identify possible magnetic phase transition due to the overlayers using a superconducting quantum interference device magnetometer (SQUID, MPMS3, Quantum Design Inc). In SQUID, the M–T curve shows weak ferromagnetism below 160 K. Element-specific X-ray magnetic circular dichroism (XMCD) measurements were performed to analyze the element-specific magnetism at 130 K, where ferromagnetism was confirmed through the bulk magnetometer.

3. Results and discussion

3.1 Crystallographic analyses

To identify the crystal structure, we measured out-of-plane XRD patterns of the samples (Fig. 2a and S2†). In the XRD pattern of as-grown SFCO (navy), diffraction peaks of 00*l* brownmillerite (BM) are observed with 00*l* LSAT substrate, indicating strong *c*-axis orientation of the film. The XRD pattern of STO overlayered SFCO (STO/SFCO, olive) looks similar to that of the as-grown SFCO. The 008$_{BM}$ peak is slightly shifted to a lower angle side. However, in the XRD pattern of NSMO overlayered SFCO (NSMO/SFCO, magenta), 002$_{BM}$, 006$_{BM}$ and 0010$_{BM}$ peaks disappeared, indicating structural transition from brownmillerite to perovskite occurred.

In order to further clarify the structural transition from brownmillerite to perovskite in NSMO/SFCO, reciprocal space mappings (RSMs) of all samples were measured (Fig. 2b). The RSM measurements were performed around the diffraction of 103 LSAT.[32] The diffraction spot of SFCO is located at the same q_x position (0.258 Å^{-1}), indicating coherent epitaxial growth occurred in all cases. Thus, the in-plane lattice constant is the same as that of LSAT (3.868 Å). The *c*-axis lattice constant of as-grown SFCO is 3.96 Å while that of the STO overlayered SFCO is 3.97 Å, indicating slight (0.25%) lattice expansion occurred by depositing STO overlayer. On the contrary, the *c*-axis lattice constant of the NSMO overlayered SFCO decreased to 3.90 Å. Structural analysis *via* XRD clearly indicates that SFCO is
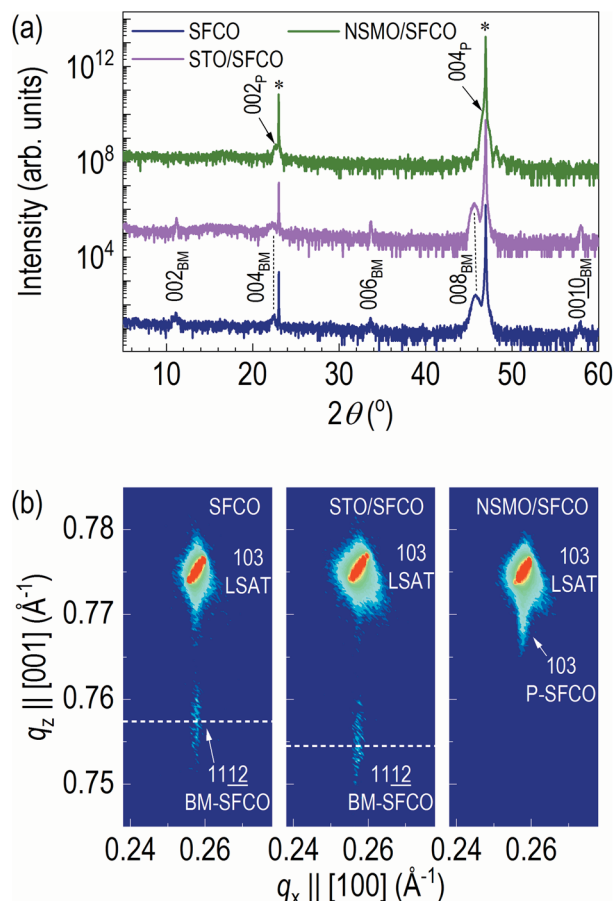
Fig. 2 (a) X-ray diffraction patterns of as-grown SFCO, STO/SFCO and NSMO/SFCO. In SFCO and STO/SFCO, the structure of SFCO shows a brownmillerite structure. The NSMO/SFCO showed a perovskite structure when the NSMO was deposited on the SFCO. (b) RSM around the diffraction spot of 103 LSAT. Each sample was grown under strain of LSAT and showed a difference in lattice constant according to the overlayers.

reduced by depositing an STO overlayer, whereas SFCO is oxidized by depositing an NSMO overlayer.

3.2 Valence state

Changes in oxide ion concentration through the overlayer enable not only structural changes but also electronic structural changes in the SFCO. Due to oxide ion movement, XAS was performed to determine the valence state of the transition metals and qualitative oxide ion concentration. Fig. 3 shows the O K edge spectra of SFCO, STO/SFCO and NSMO/SFCO. Additionally, we measured XAS spectra of single layered STO and NSMO thin films to identify the origin of peaks in O K edge spectra from SFCO, STO/SFCO, and NSMO/SFCO. Fig. 3a shows an O K edge spectrum of as-grown SFCO thin film in brownmillerite. As the overlayer changes, the shapes of signals show a clear change. Fig. 3b shows an O K edge spectrum of STO/SFCO. We added XAS spectra from individual SFCO and STO thin films. There is no drastic change in the O K edge spectrum of STO/SFCO. However, peaks that were not present in that of
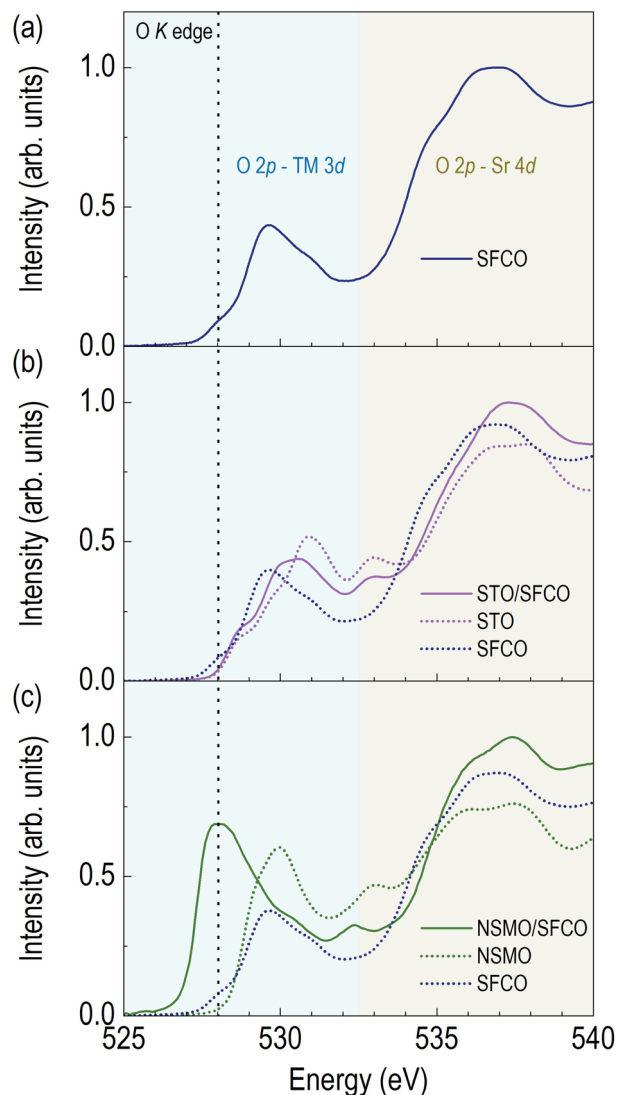

Fig. 3 XAS data of the O K edges of (a) as-grown SFCO (navy solid line), (b) STO/SFCO (magenta solid line) and (c) NSMO/SFCO (olive solid line) were performed to track the change in oxide ion according to the overlayer. In order to clarify the change of the O K edge spectrum due to of the overlayer, the O K edge spectra of the SFCO, STO and NSMO are indicated by dotted lines. In NSMO/SFCO, the hybridization of TM 3d−O 2p was increased.

SFCO are clearly seen at 531 and 533 eV in STO/SFCO. From the comparison with that of an STO film, they are mainly contributed from STO. Lastly, in Fig. 3c, a large peak at the pre-edge region of O K edge (vertical black dotted line at about 528 eV) from the spectrum of NSMO/SFCO was observed. The pre-edge peak from O K edge spectra is related to O 2p–TM 3d hybridization, and the intensity is related to the strength of hybridization.[33] The peak cannot be explained by the contribution from the O K edge spectrum of Mn–O hybridization, which is indicated by green-colored dotted line. In the XAS of SFCO, the peak at 528 eV is very weak. This means smaller O 2p–TM 3d hybridization in the brownmillerite due to the smaller number of available oxygen atoms around transition metals. On the other hand, in the spectrum of NSMO/SFCO, a large signal is

found at around 528 eV, which shows an increase in oxygen content.[33,34] A decrease in peak intensity in the O K edge spectrum of STO/SFCO indicates the removal of oxide ions in SFCO. Changes in oxygen ion concentration are shown by comparing the O K edges of each sample. When two complex metal oxides form an interface through overlayer deposition, the oxygen ion concentration changes rather than simply having two layers.

Fig. 4a shows XAS spectra around Fe L edge. The peak position of Fe L_3 edge of the SFCO is located at 709.15 eV. The peak of the STO/SFCO is located at 709.20 eV, close to that of the SFCO. However, the peak of the NSMO/SFCO is located at 709.30 eV, where 0.15 eV higher than that of the SFCO. The 0.15 eV difference seen in the NSMO/SFCO suggests an increase in Fe valence state.[35–37] It also shows the broadening of the peak in the high energy side of the Fe L_2 edge, which means an increase in the Fe^{4+} state in the Fe valence state.[37] In addition, changes in the relative intensities in two peaks at Fe L_2 edge can be considered as the increase of Fe valency in the NSMO/SFCO. The shape of the Fe L_2 edge is similar to the previously reported $SrFeO_3$.[33,35,37] The increase in the peak position through Fe L_3 edge and broadening of the peak in the high energy side of the

Fe L_2 edge show that the NSMO overlayer increases the valence state of Fe.

Fig. 4b shows XAS spectra around Co L edge. Oxide ion concentration can be inferred from valence states of TMs. The Co L_3 edge of SFCO is located at 779.20 eV. Although there is no difference between the SFCO and STO/SFCO, the Co L_3 edge of the NSMO/SFCO locates a higher energy side (779.45 eV), clearly indicating that NSMO overlayer oxidized SFCO. Next, in order to
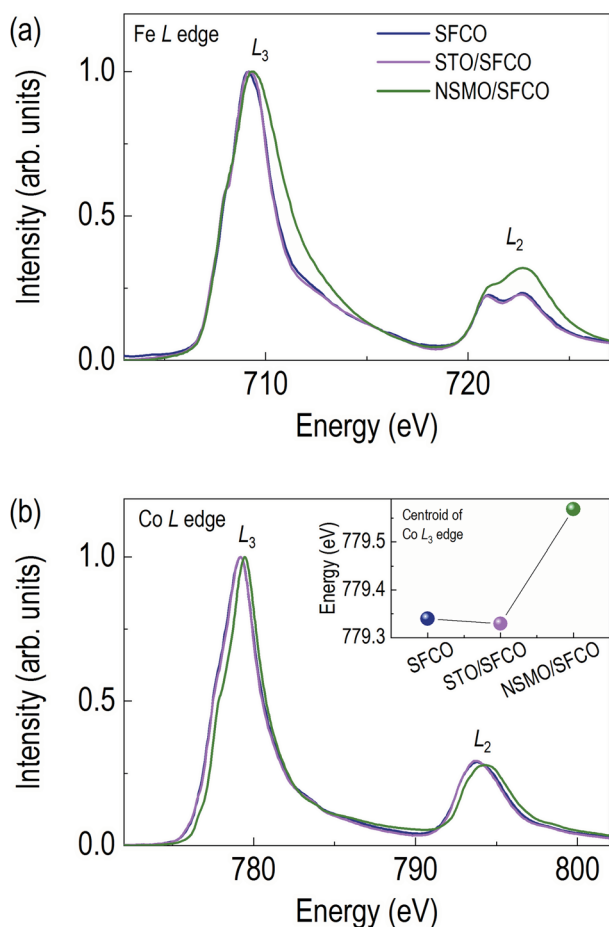

Fig. 4 (a) XAS of Fe L edge and (b) Co L edge in SFCO, STO/SFCO and NSMO/SFCO. Fe L edge spectra shows an increase in Fe^{3+} in NSMO/SFCO. The spectral centroid for comparing the Co L edge are included in the inset of (b). The valence of TM is lowered through the STO overlayer and increased through the NSMO overlayer.

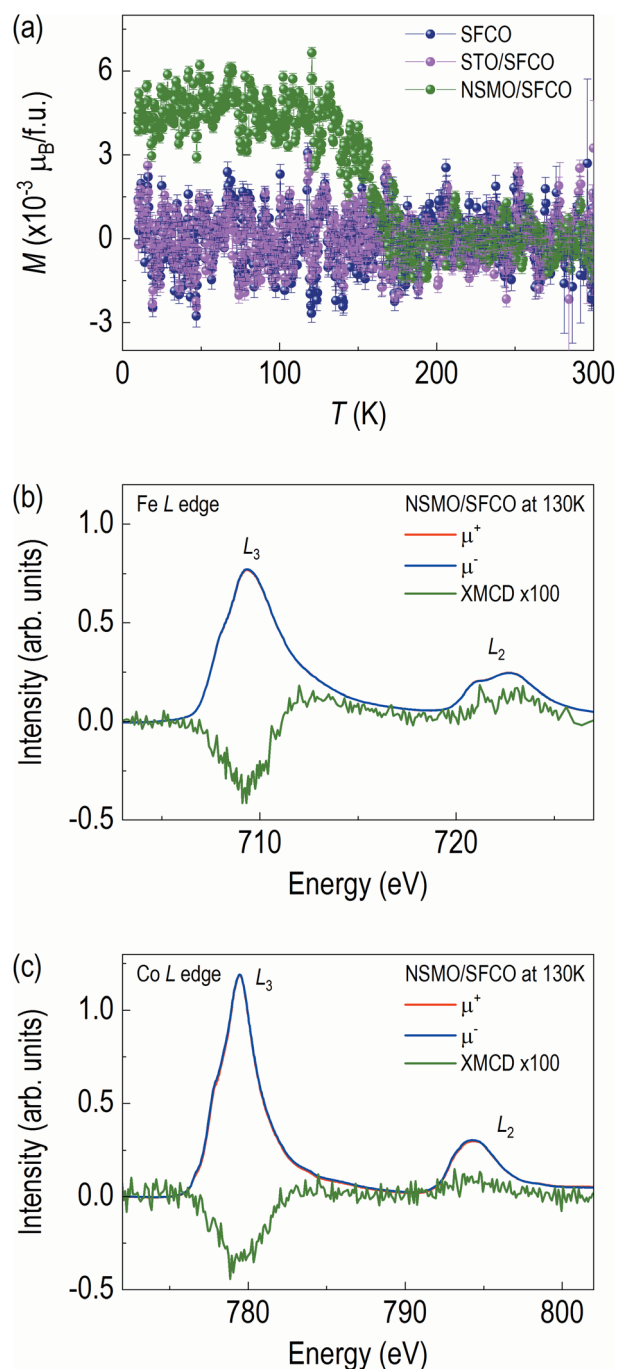**Fig. 5** (a) Magnetization *vs.* temperature graph of SFCO, STO/SFCO, and NSMO/SFCO. NSMO/SFCO shows ferromagnetism below 160 K. To find the origin of the ferromagnetism of NSMO/SFCO, element-specific XMCD of (b) Fe and (c) Co L edges was measured.

clearly see the differences in the Co L_3 edge peak position of SFCO and STO/SFCO in detail, we compared the spectral centroid value of the Co L_3 edge (inset of Fig. 4b). The spectral centroid of Co L_3 edge of STO/SFCO shows 0.01 eV reduction compared to SFCO, indicating an oxygen reduction of SFCO occurred by depositing STO overlayer, most likely due to STO extracts oxide ion from SFCO.[38] From the Co L edge spectra, it can be seen that the STO overlayer reduces SFCO while the NSMO overlayer oxidizes SFCO.

3.3 Magnetism

SFCO system shows change in the magnetic properties from antiferromagnetic to ferromagnetic upon structural transition from brownmillerite to perovskite.[13,39–41] We measured the magnetic properties at low temperatures (Fig. 5). The M–T curve of the NSMO/SFCO shows a clear upturn around 160 K (Fig. 5a), indicating ferromagnetic properties, though the SFCO and the STO/SFCO do not show any phase transition in the range of temperature we measured.

Since the noise level of the M–T curves is quite large, we further measured grazing angle XMCD spectra at 130 K with 0.5 T (Fig. 5b and c) to confirm the ferromagnetism of the NSMO/SFCO. Ferromagnetic XMCD signals from Fe L edge and Co L edge are clearly seen. Note we also measured XMCD of Mn L edge and O K edge, however no XMCD signals were detected (Fig. S3†). The XMCD features of Fe L edge and Co L edge are similar in shape, meaning spin polarization direction are parallel. The signals from Fe L edge and Co L edge clearly demonstrate that the NSMO/SFCO shows weak ferromagnetism.

3.4 Discussion

Here we would like to discuss the mechanism of the reduction/oxidation of SFCOs by the overlayer deposition. We focused on the oxygen vacancy formation energy (E_{OV}) because E_{OV} represents the energy required to form oxygen vacancy. E_{OV} of NSMO is 1.78 eV (ref. 42) while that of STO is 5.54 eV (ref. 43 and 44). STO is known as an oxide ion getter material that extracts oxide ions from SFCO.[38] Although there is no data of E_{OV} for SFCO, we assumed the E_{OV} of SFCO is 2.95 eV because the E_{OV} of $SrCoO_{2.5}$ is 2.90 eV (ref. 45) and that of $SrFeO_{2.5}$ is 3.00 eV (ref. 46). $E_{OV}(SFCO) - E_{OV}(NSMO)$ is ~+1.17 eV and $E_{OV}(SFCO) - E_{OV}(STO)$ is ~−2.59 eV. Thus, oxide ions in NSMO are removed by SFCO while STO removes oxide ions from SFCO. Therefore, the oxide ion concentration in SFCO is changed during the overlayer growth due to oxidation or reduction originated from the difference in the chemical potential. By growing an overlayer on the interface of a complex oxide material, new possibilities for catalytic activity or ion-driven technology can be presented.[47,48]

4. Conclusions

In conclusion, selective deposition of an overlayer on the SFCO oxygen sponge can control the oxide ion concentration. We fabricated SFCOs followed by the deposition of two kinds of complex oxides (STO, NSMO) under exactly the same growth condition. Oxide ion movement through the heterointerface

between overlayer/SFCO was tracked by the observation of the changes in the crystal structure, valence state, and magnetic ground state. The crystal structure of SFCO changed from brownmillerite to perovskite when NSMO was deposited as the overlayer while brownmillerite structure was kept when STO was deposited. We showed spectroscopic evidence of redox activity through bilayer interfaces, which supported by the energy difference. Due to the difference in E_{OV}s, oxygen vacancies in SFCO are easily generated in STO/SFCO ($\Delta E_{OV} \sim -2.59$ eV), while oxygen absorption from NSMO occurs in NSMO/SFCO ($\Delta E_{OV} \sim 1.17$ eV). Further, the NSMO/SFCO showed weak ferromagnetism. From these observations, the oxide ion concentration in SFCO is changed during the overlayer growth due to oxidation or reduction originated from the difference in the chemical potential. The present results might be useful to design advanced ionic devices using TM-based perovskite oxides.

Conflicts of interest

There are no conflicts to declare.

Acknowledgements

References

1 D. I. Khomskii and G. A. Sawatzky, *Catal. Lett.*, 1997, **102**, 87.
2 E. Dagotto, *Science*, 2005, **309**, 257.
3 J. B. Torrance, P. Lacorre, A. I. Nazzal, E. J. Ansaldo and C. Niedermayer, *Phys. Rev. B: Condens. Matter Mater. Phys.*, 1992, **45**, 8209.
4 H. Y. Hwang, S. W. Cheong, P. G. Radaelli, M. Marezio and B. Batlogg, *Phys. Rev. Lett.*, 1995, **75**, 914.
5 Y. Moritomo, Y. Tomioka, A. Asamitsu, Y. Tokura and Y. Matsui, *Phys. Rev. B: Condens. Matter Mater. Phys.*, 1995, **51**, 3297.
6 C. Leighton, *Nat. Mater.*, 2019, **18**, 13.
7 D. G. Schlom, L. Q. Chen, C. B. Eom, K. M. Rabe, S. K. Streiffer and J. M. Triscone, *Annu. Rev. Mater. Res.*, 2007, **37**, 589.
8 J. J. Yang, M. D. Pickett, X. M. Li, D. A. A. Ohlberg, D. R. Stewart and R. S. Williams, *Nat. Nanotechnol.*, 2008, **3**, 429.
9 R. Waser, R. Dittmann, G. Staikov and K. Szot, *Adv. Mater.*, 2009, **21**, 2632.
10 U. Bauer, L. Yao, A. J. Tan, P. Agrawal, S. Emori, H. L. Tuller, S. van Dijken and G. S. D. Beach, *Nat. Mater.*, 2015, **14**, 174.
11 D. A. Gilbert, J. Olamit, R. K. Dumas, B. J. Kirby, A. J. Grutter, B. B. Maranville, E. Arenholz, J. A. Borchers and K. Liu, *Nat. Commun.*, 2016, **7**, 11050.
12 Q. Y. Lu and B. Yildiz, *Nano Lett.*, 2016, **16**, 1186.
13 H. Jeen, W. S. Choi, M. D. Biegalski, C. M. Folkman, I. C. Tung, D. D. Fong, J. W. Freeland, D. Shin, H. Ohta, M. F. Chisholm and H. N. Lee, *Nat. Mater.*, 2013, **12**, 1057.

14 J. Gazquez, S. Bose, M. Sharma, M. A. Torija, S. J. Pennycook, C. Leighton and M. Varela, *APL Mater.*, 2013, **1**, 012105.

15 A. P. Ramirez, *J. Phys.: Condens. Matter*, 1997, **9**, 8171.

16 J. H. Park, E. Vescovo, H. J. Kim, C. Kwon, R. Ramesh and T. Venkatesan, *Nature*, 1998, **392**, 794.

17 Y. M. Kim, J. He, M. D. Biegalski, H. Ambaye, V. Lauter, H. M. Christen, S. T. Pantelides, S. J. Pennycook, S. V. Kalinin and A. Y. Borisevich, *Nat. Mater.*, 2012, **11**, 888.

18 G. A. Niklasson and C. G. Granqvist, *J. Mater. Chem.*, 2007, **17**, 127.

19 U. Guth, W. Vonau and J. Zosel, *Meas. Sci. Technol.*, 2009, **20**, 042002.

20 P. Calka, M. Sowinska, T. Bertaud, D. Walczyk, J. Dabrowski, P. Zaumseil, C. Walczyk, A. Gloskovskii, X. Cartoixa, J. Sune and T. Schroeder, *ACS Appl. Mater. Interfaces*, 2014, **6**, 5056.

21 X. L. Xu, H. Zhang, Z. C. Zhong, R. R. Zhang, L. H. Yin, Y. P. Sun, H. L. Huang, Y. L. Lu, Y. Lu, C. Zhou, Z. W. Ma, L. Shen, J. S. Wang, J. D. Guo, J. R. Sun and Z. G. Sheng, *ACS Appl. Mater. Interfaces*, 2020, **12**, 31645.

22 M. Nord, P. E. Vullum, M. Moreau, J. E. Boschker, S. M. Selbach, R. Holmestad and T. Tybell, *Appl. Phys. Lett.*, 2015, **106**, 041604.

23 E. J. Guo, Y. H. Liu, C. Sohn, R. D. Desautels, A. Herklotz, Z. L. Liao, J. Nichols, J. W. Freeland, M. R. Fitzsimmons and H. N. Lee, *Adv. Mater.*, 2018, **30**, 1705904.

24 J. S. Hong, A. N. Aphale, S. J. Heo, B. X. Hu, M. Reisert, S. Belko and P. Singh, *ACS Appl. Mater. Interfaces*, 2019, **11**, 34878.

25 D. Lee, Y. L. Lee, A. Grimaud, W. T. Hong, M. D. Biegalski, D. Morgan and Y. Shao-Horn, *J. Phys. Chem. C*, 2014, **118**, 14326.

26 W. S. Choi, H. Jeen, J. H. Lee, S. S. A. Seo, V. R. Cooper, K. M. Rabe and H. N. Lee, *Phys. Rev. Lett.*, 2013, **111**, 097401.

27 Q. Yang, H. J. Cho, H. Jeen and H. Ohta, *J. Appl. Phys.*, 2021, **129**, 215303.

28 Q. Yang, H. J. Cho, H. Jeen and H. Ohta, *Adv. Mater. Interfaces*, 2019, **6**, 1901260.

29 N. P. Lu, P. F. Zhang, Q. H. Zhang, R. M. Qiao, Q. He, H. B. Li, Y. J. Wang, J. W. Guo, D. Zhang, Z. Duan, Z. L. Li, M. Wang, S. Z. Yang, M. Z. Yan, E. Arenholz, S. Y. Zhou, W. L. Yang, L. Gu, C. W. Nan, J. Wu, Y. Tokura and P. Yu, *Nature*, 2017, **546**, 124.

30 J. Lee, E. Ahn, Y. S. Seo, Y. Kim, T. Y. Jeon, J. Cho, I. Lee and H. Jeen, *Phys. Rev. Appl.*, 2018, **10**, 054035.

31 P. D. Battle, T. C. Gibb and P. Lightfoot, *J. Solid State Chem.*, 1988, **76**, 334.

32 A. Khare, J. Lee, J. Park, G. Y. Kim, S. Y. Choi, T. Katase, S. Roh, T. S. Yoo, J. Hwang, H. Ohta, J. Son and W. S. Choi, *ACS Appl. Mater. Interfaces*, 2018, **10**, 4831.

33 V. R. Galakhov, E. Z. Kurmaev, K. Kuepper, M. Neumann, J. A. McLeod, A. Moewes, I. A. Leonidov and V. L. Kozhevnikov, *J. Phys. Chem. C*, 2010, **114**, 5154.

34 L. Karvonen, M. Valkeapaa, R. S. Liu, J. M. Chen, H. Yamauchi and M. Karppinen, *Chem. Mater.*, 2010, **22**, 70.

35 M. Abbate, G. Zampieri, J. Okamoto, A. Fujimori, S. Kawasaki and M. Takano, *Phys. Rev. B: Condens. Matter Mater. Phys.*, 2002, **65**, 165120.

36 A. Koehl, D. Kajewski, J. Kubacki, C. Lenser, R. Dittmann, P. Meuffels, K. Szot, R. Waser and J. Szade, *Phys. Chem. Chem. Phys.*, 2013, **15**, 8311.

37 M. Abbate, F. M. F. de Groot, J. C. Fuggle, A. Fujimori, O. Strebel, F. Lopez, M. Domke, G. Kaindl, G. A. Sawatzky, M. Takano, Y. Takeda, H. Eisaki and S. Uchida, *Phys. Rev. B: Condens. Matter Mater. Phys.*, 1992, **46**, 4511.

38 J. D. Ferguson, Y. Kim, L. F. Kourkoutis, A. Vodnick, A. R. Woll, D. A. Muller and J. D. Brock, *Adv. Mater.*, 2011, **23**, 1226.

39 Y. Tsujimoto, C. Tassel, N. Hayashi, T. Watanabe, H. Kageyama, K. Yoshimura, M. Takano, M. Ceretti, C. Ritter and W. Paulus, *Nature*, 2007, **450**, 1062.

40 S. Srinath, M. M. Kumar, K. Sahner, M. L. Post, M. Wickles, R. Moos and H. Srikanth, *J. Appl. Phys.*, 2006, **99**, 08S904.

41 A. Munoz, C. de la Calle, J. A. Alonso, P. M. Botta, V. Pardo, D. Baldomir and J. Rivas, *Phys. Rev. B: Condens. Matter Mater. Phys.*, 2008, **78**, 054404.

42 Y. Zhou, Z. Lu, S. Xu, D. Xu and Z. Yang, *Fuel Cells*, 2015, **15**, 839.

43 L. P. Zhang, B. Liu, H. L. Zhuang, P. R. C. Kent, V. R. Cooper, P. Ganesh and H. X. Xu, *Comput. Mater. Sci.*, 2016, **118**, 309.

44 R. Astala and P. D. Bristowe, *Modell. Simul. Mater. Sci. Eng.*, 2001, **9**, 415.

45 Y. U. Shi, R. J. Xie, X. T. Liu, N. A. Zhang, C. Aruta and N. Yang, *Phys. Chem. Chem. Phys.*, 2019, **21**, 16230.

46 T. Das, J. D. Nicholas and Y. Qi, *J. Mater. Chem. A*, 2017, **5**, 4493.

47 M. Minakshi, N. Sharma, D. Ralph, D. Appadoo and K. Nallathamby, *Electrochem. Solid-State Lett.*, 2011, **14**, A86.

48 M. M. Sundaram, T. Watcharatharapong, S. Chakraborty, R. Ahuja, S. Duraisamy, P. T. Rao and N. Munichandraiah, *Dalton Trans.*, 2015, **44**, 20108.